Personalized Radiotherapy Planning for Glioma Using Multimodal Bayesian Model Calibration

Jana Lipková^{a,1}, Panagiotis Angelikopoulos^b, Stephen Wu^c, Esther Alberts^e, Benedikt Wiestler^e, Christian Diehl^e, Christine Preibisch^f, Thomas Pyka^g, Stephanie Combs^h, Panagiotis Hadjidoukas^d, Koen Van Leemputⁱ, Petros Koumoutsakos^d, John S. Lowengrub^j, and Bjoern Menze^a

^aDepartment of Informatics, TU Munich, Germany; ^bD.E. Shaw Research, L.L.C, USA; ^cInstitute of Statistical Mathematics, Tokyo, Japan; ^dComputational Science and Engineering Laboratory, ETH Zürich, Switzerland; ^eDepartment of Neuroradiology, Klinikum Rechts der Isar, TU Munich, Germany; ^fDepartment of Diagnostic and Interventional Neuroradiology & Neuroimaging Center & Clinic for Neurology, Klinikum Rechts der Isar, TU Munich; ^gDepartment of Nuclear Medicine, Klinikum Rechts der Isar, TU Munich; ^hDepartment of Radiation Oncology, Klinikum Rechts der Isar, TU Munich & Institute of Innovative Radiotherapy, Helmholtz Zentrum Munich & Deutsches Konsortium für Translationale Krebsforschung, Partner Site Munich; ^hHarvard Medical School, Boston, MA,USA & Department of Applied Mathematics and Computer Science, TU Denmark, Denmark; ^hDepartment of Mathematics & Center for Complex Biological Systems & Chao Family Comprehensive Cancer Center, UC Irvine, USA

This manuscript was compiled on July 2, 2018

Existing radiotherapy (RT) plans for brain tumors derive from population studies and scarcely account for patient-specific conditions. We propose a personalized RT design through the combination of patient multimodal medical scans and state-of-the-art computational tumor models. Our method integrates complementary information from high-resolution MRI scans and highly specific FET-PET metabolic maps to infer tumor cell density in glioma patients. The present methodology relies on data from a single time point and thus is applicable to standard clinical settings. The Bayesian framework integrates information across multiple imaging modalities, quantifies imaging and modelling uncertainties, and predicts patient-specific tumor cell density with confidence intervals. The computational cost of Bayesian inference is reduced by advanced sampling algorithms and parallel software. An initial clinical population study shows that the RT plans generated from the inferred tumor cell infiltration maps spare more healthy tissue thereby reducing radiation toxicity while yielding comparable accuracy with standard RT protocols. Moreover, the inferred regions of high tumor cell density coincide with the tumor radio-resistant areas, providing guidance for personalized dose escalation. The proposed integration of data and models provides a robust, non-invasive tool to assist personalized RT planning.

Glioblastoma | Bayesian inference | Radiotherapy planning | FET-PET

lioblastoma (GBM) is the most aggressive and most common type of primary brain tumor, with a median survival of only 15 months under treatment (1). The standard treatment consists of immediate tumor resection, followed by combined radio- and chemotherapy targeting tumor residuals. All treatment procedures are guided by magnetic resonance imaging (MRI), mainly T1 gadolinium enhanced (T1Gd) and fluid attenuation inversion recovery (FLAIR) scans. T1Gd enhances vascularized parts of the tumor, while FLAIR shows surrounding tumor edema. In contrast to most tumors, GBM infiltrates the surrounding tissue, instead of forming a tumor with a well-defined boundary. The central tumor, which is visible in the standard morphological images, is commonly resected. However, the question of where the nearby tissue is highly infiltrated by tumor cells, and as such is likely to be the location of a later progression, remains unanswered.

Current radiotherapy (RT) planning is handling these uncertainties in a rather rudimentary fashion. The irradiated volume, referred to as clinical target volume (CTV), is designed by extending the visible tumor region by a uniform margin to account for the invisible tumor infiltration. However, the extent of this margin varies by a few centimeters even across

the official RT guidelines (2). Moreover, GBM invasiveness is highly patient-specific, and thus not all patients benefit equally from the same margin. Finally, a uniform margin might not provide an optimal dose distribution for complex anisotropically growing tumors.

Despite treatment almost all GBMs undergo recurrence (3). Biopsies (4) and a post-mortem studies (5) show that an incomplete tumor coverage by the CTV is a possible cause of RT inefficiency. At the same time radio-resistance of tumor residuals inside the CTV can further reduce RT efficiency. Tumor radio-resistance appears in regions with complex microenviroment and hypoxia (6), both commonly encountered in areas of high tumor cellularity. To address the tumor radio-resistance, several studies have suggested a local dose escalation (6–8). A boosted dose is usually delivered into a single or multiple co-centered regions defined by uniform margins added to the tumor outlines visible in MRI (9). The Radiation Therapy Oncology Group (RTOG) phase-I-trial (8) showed an increase in median survival of 8 months with dose escalation. However, no benefit in a progression-free survival was observed, indicating a complex relation between the true progression of the underlying disease and the tumor extent visible in MRI scans.

Positron emission tomography (PET) scans offer means to directly map tumor metabolic activities using targeted tracers. A promising tracer used in GBM imaging is 18F-fluoro-ethyltyrosine (FET) (10), whose uptake values are proportional

Significance Statement

We demonstrate that patient-specific, data driven modeling extends the capabilities of personalized radiotherapy (RT) design for infiltrative brain tumors. We combine patient-specific structural and metabolic scans from a single time point with a computational tumor growth model through a Bayesian inference framework and predict the tumor distribution beyond its outlines visible in medical images. These predictions enable personalized RT designs with improved delineation of tumor regions and identified radio-resistant areas. In turn the ensuing RT spares healthy tissue and reduces radiation toxicity, while reaching comparable accuracy with standard RT protocols.

Author contributions: J.L. research execution; P.A.,S.W.,P.H.,P.K.,K.V.L., Bayesian analysis support; E.A.,B.W.,C.D.,T.P.,C.P.,S.C. data acquisition/processing; B.M., J.S.L., P.K. research organization

The authors declare no conflict of interest.

¹To whom correspondence should be addressed. E-mail: jana.lipkova@tum.de

to tumor cell density (11). A prospective phase II study (3) demonstrated that dose escalation based on FET-PET enhancement delineates the tumor structure better than uniform margins, thus leading to lower radiation toxicity. Still, it did not increase the progression-free survival. One possible explanation is that FET scan shows a baseline signal also in normal tissue, which together with the rather poor resolution of PET limits its ability to distinguish between healthy and normal tissue in regions of low infiltration in the tumor periphery. The standard RT plans can be improved by incorporating infor-

mation from computational tumor models (12, 13). Most brain tumor growth models are based on the Fisher-Kolmogorov (FK) equation (14). These models, calibrated against patient medical scans, provide estimates of tumor infiltration that extend the information available in medical images and can guide the personalized RT designs. Despite great advances in the design of tumor growth models (14–18) critical questions remains for the applicability of these models, such as how to link model features (e.g. tumor cell density) to clinical image observations. Current approaches for calibrating glioma models consider various deterministic (13, 14, 19, 20) and probabilistic Bayesian (21, 22) methods for establishing this link. In (13, 14, 19-21), authors assume a fixed tumor cell density at the tumor borders visible in T1Gd and FLAIR scans and the model parameters are estimated by fitting the volume (19, 20) or shape (13, 21) of the visible lesion. However, the tumor cell density varies along the visible tumor outlines due to anatomical restrictions and inhomogeneous growth pattern. A Bayesian approach accounting for varying tumor cell density was proposed in (22). All these calibrations however use MRI scans from at least two time points, making them unsuitable for real clinical setting, where only scans acquired at single preoperative time point are available.

In this paper we present a systematic Bayesian framework to develop robust tumor growth models informed from clinical imaging features. Our approach overcomes limitations specific to different imaging modalities and in turn integrates their information to calibrate the tumor growth models for the RT planning. We combine complementary information from structural MRI and functional FET-PET metabolic maps, acquired at a single time point, to identify the patient-specific tumor cell density. Our Bayesian approach infers modeling and imaging parameters under uncertainties arising from measurement and modeling errors. We propagate these uncertainties to model predictions to obtain robust estimates of the tumor cell density together with confidence intervals that can be used for personalized RT planning. The estimated patient-specific tumor cell density offers an advantage in determining margins of the CTV as well as regions for dose escalation. A study conducted on a small clinical population is used to assess the benefits of the personalized RT plans over standard protocols.

1. Bayesian model personalization

The tumor cell density $\mathbf{u}(\theta_u|M_u)$ is computed by a model M_u with parameters θ_u . The parameters θ_u are patient-specific and a probability distribution of their plausible values is inferred from tumor observations (data) $\mathcal{D} := \{\hat{\mathbf{y}}^k\}_{k=1}^S$ obtained from S medical scans. We postulate that the model predictions **u** and each image observation $\hat{\mathbf{y}}^k$ are related by a stochastic imaging model \mathcal{F}^k with parameters $\theta_{\mathcal{F}^k}$ as

$$\hat{\mathbf{y}}^k = \mathcal{F}^k \left(\mathbf{u} \left(\theta_u | M_u \right), \varepsilon \left(\theta_{\mathcal{F}^k} \right) \right),$$
 [1]

where ε is a prediction error accounting for modelling and measurement uncertainties. Parameters $\theta := \{\theta_u, \theta_{\mathcal{F}^1}, \cdots, \theta_{\mathcal{F}^S}\}$ of the model $M := \{M_u, M_{\mathcal{F}^1}, \cdots, M_{\mathcal{F}^S}\}$ are assumed to be unknown.

A. Parameters estimation and uncertainty propagation. A prior probability distribution function (PDF) $\mathbb{P}(\theta|M)$ is used to incorporate any prior information about θ . Bayesian model calibration updates this prior information based on the available data \mathcal{D} . The updated posterior PDF is computed by the Bayes theorem:

$$\mathbb{P}(\theta|\mathcal{D}, M) \propto \mathbb{P}(\mathcal{D}|\theta, M) \cdot \mathbb{P}(\theta|M),$$
 [2]

where $\mathbb{P}(\mathcal{D}|\theta, M)$ is the *likelihood* of observing data \mathcal{D} from the model M for a given value of θ . In most cases an analytical expression for Eq. (2) is not available and sampling algorithms are used to obtain sample $\theta^{(l)}$, $l \in \{1, \dots, N\}$ from the posterior $\mathbb{P}(\theta|\mathcal{D}, M)$. We used a Transitional Markov Chain Monte Carlo (TMCMC) sampling algorithm (23), which iteratively constructs a series of intermediate PDFs:

$$\mathbb{P}_{i}(\theta|\mathcal{D}, M) \sim \mathbb{P}(\mathcal{D}|\theta, M)^{p_{j}} \cdot \mathbb{P}(\theta|M),$$
 [3]

where $0 = p_0 < p_1 < \dots < p_m = 1 \text{ and } j = \{1, \dots, m\} \text{ is a}$ generation index. The term p_i controls the convergence of the sampling procedure and is computed automatically by the TMCMC algorithm. TMCMC constructs a large number of independent chains that explore parameter space more efficiently than traditional sampling methods (23) and allow parallel execution. A highly parallel implementation of the TMCMC algorithm is provided by the $\Pi 4U$ framework (24). The inferred parametric uncertainties are propagated through the model M to obtain robust posterior predictions about \mathbf{u} , given by the PDF:

$$\mathbb{P}(\mathbf{u}|\mathcal{D}, M) = \int_{\Theta} \mathbb{P}(\mathbf{u}|\theta, M) \cdot \mathbb{P}(\theta|\mathcal{D}, M) d\theta,$$
 [4]

or by simplified measures such as the mean $\mu_{\mathbf{u}} = E[\mathbf{u}(\theta)] \equiv m_1$ and variance $\sigma_{\mathbf{u}}^2 = E[\mathbf{u}^2(\theta)] - m_1^2 \equiv m_2 - m_1^2$, derived from the first two moments m_k , k=1,2:

$$m_k = \int_{\Theta} \left(\mathbf{u}(\theta|M) \right)^k \cdot \mathbb{P}(\theta|\mathcal{D}, M) \, d\theta \approx \frac{1}{N} \sum_{l=1}^N \left(\mathbf{u}(\theta^{(l)}|M) \right)^k, \quad [5]$$

where Θ denotes the space of all uncertain parameters.

B. Tumor growth model. Tumor models of various complexity can be personalized using the Bayesian approach described above. Here, we model $\mathbf{u}(\theta_u|M_u)$ with the FK model which describes anisotropic tumor growth in the brain $\Omega \in \mathbb{R}^3$ as:

$$\begin{array}{lcl} \frac{\partial \mathbf{u}}{\partial t} & = & \nabla \cdot \left(\mathbb{D} \, \nabla \mathbf{u} \right) + \rho \mathbf{u} \left(1 - \mathbf{u} \right), & in \, \Omega & \quad [6] \\ \nabla \mathbf{u} \cdot \vec{n} & = & 0, & in \, \partial \Omega, & \quad [7] \end{array}$$

$$\nabla \mathbf{u} \cdot \vec{n} = 0, \quad in \ \partial \Omega, \tag{7}$$

where $\mathbf{u} = \{u_i(t)\}_{i=1}^{\#Voxels}$ and $u_i(t) \in [0,1]$ is a normalized tumor cell density at time t and voxel $i = (i_x, i_y, i_z) \in \Omega$. The term $\rho \left[1/day \right]$ denotes tumor proliferation rate. The tumor infiltration into the surrounding tissues is modeled by the tensor $\mathbb{D}=\{D_i\,\mathbb{I}\}_{i=1}^{\#\textit{Voxels}}$ where \mathbb{I} is a 3×3 identity matrix and

$$D_{i} = \begin{cases} D_{g} & \text{if } i \in \Omega_{gray}, \\ D_{w} & \text{if } i \in \Omega_{white}, \\ 0 & \text{if } i \notin \Omega_{gray} \cup \Omega_{white}. \end{cases}$$
 [8]

The terms D_w and D_g denote tumor infiltration in white and gray matter and we assume $D_w = 10D_q \left[mm^2/day\right]$ (12). The

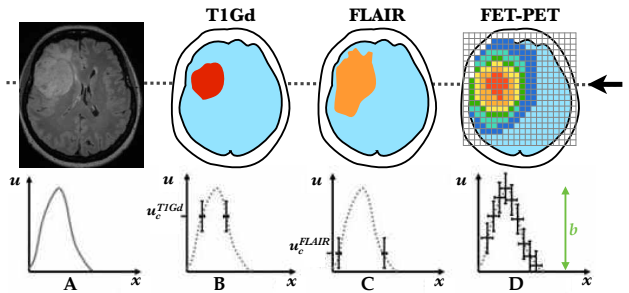


Fig. 1. Schematic illustrating the relation between the image observations \mathcal{D} (top) and the tumor cell density \mathbf{u} (bottom). **A**: Actual FLAIR scan and schematic of the tumor cell density along the line indicated by the black arrow. **B,C**: Binary segmentations of the visible tumor and their relation to the unknown threshold values u_c^{TIGd} , u_c^{FLAIR} . **D**: FET-PET metabolic map and the unknown constant of proportionality b.

ventricles and skull are not infiltrated by the tumor and act as a domain boundary with an imposed no-flux boundary condition Eq. (7), where \vec{n} is the outward unit normal to $\partial\Omega$. The tumor is initialized at voxel (ic_x,ic_y,ic_z) and its growth is modeled from time t=0 until detection time t=T [day]. The model parameters $\theta_u \equiv \{D_w, \rho, T, ic_x, ic_y, ic_z\}$ are considered unknown and patient-specific. The model M_u is implemented in a 3D extension of the multi-resolution adapted grid solver (25) with typical simulation time 1-3 minutes with 2 cores.

C. Multimodal imaging model. We extract the tumor information from T1Gd and FLAIR MRI and metabolic FET-PET maps. The MRI scans provide morphological information about the visible tumor in the form of binary segmentations. The FET signal is proportional to tumor cell density with an unknown constant of proportionality (11). A relation between the image observations $\mathcal{D} = \{\hat{\mathbf{y}}^{TIGd}, \hat{\mathbf{y}}^{FLAIR}, \hat{\mathbf{y}}^{FET}\}$ and tumor cell density \mathbf{u} is sketched in Fig. 1. Since each of the scans capture a different physiological process, the observations are assumed independent and the likelihood can be express as:

$$\mathbb{P}(\mathcal{D}|\theta,M) = \mathbb{P}\left(\hat{\mathbf{y}}^{^{TIGd}}|\theta,M\right)\mathbb{P}\left(\hat{\mathbf{y}}^{^{FLAIR}}|\theta,M\right)\mathbb{P}\left(\hat{\mathbf{y}}^{^{FET}}|\theta,M\right).$$

A stochastic imaging model \mathcal{F}^k is used to define the likelihood function for each modality $\hat{\mathbf{y}}^k$. The binary segmentations $\hat{\mathbf{y}}^s, s \in \{T1Gd, FLAIR\}$, assign a label $y_i^s = 1$ to each voxel with visible tumor and $y_i^s = 0$ otherwise. The probability of observing a segmentation $\hat{\mathbf{y}}^s$ with a simulated tumor cell density \mathbf{u} is assumed as a Bernoulli distribution (22):

$$\mathbb{P}(\hat{\mathbf{y}}^s|\theta, M) = \prod_{i=1}^{N_{y^s}^d} \mathbb{P}(y_i^s|\theta, u_i) = \prod_{i=1}^{N_{y^s}^d} \alpha_i^{y_i^s} \cdot (1 - \alpha_i)^{1 - y_i^s}.$$
[9]

Here α_i is the probability of observing the tumor in the MRI scan and it is assumed as a double logistic sigmoid:

$$\alpha_i(u_i, u_c^s) = 0.5 + 0.5 \cdot \text{sign}(u_i - u_c^s) \left(1 - e^{-\frac{(u_i - u_c^s)^2}{\sigma_\alpha^2}} \right), \quad [10]$$

where u_c^s denotes an unknown cell density threshold below which tumor induced changes are not visible in the MRI scan, while the term σ_{α}^2 represents uncertainty in u_c^s . The parameter $N_{y^s}^d$ denotes the set of voxels used for the likelihood computation. The MRI scans were acquired at uniform $1\,mm$ resolution. To cope with potential correlations between neighbouring voxels, only every second voxel is included in $N_{y^s}^d$, introducing a correlation length $d=2\,mm$. The binary segmentations have three unknown parameters

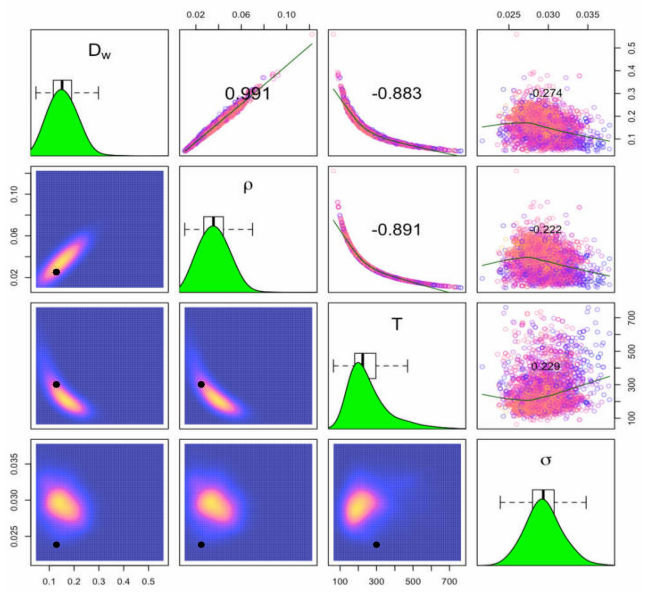


Fig. 2. The results of the Bayesian calibration for the synthetic case. Above the diagonal: Projection of the TMCMC samples of the posterior distribution $\mathbb{P}(\theta|\mathcal{D},M)$ in 2D space of the selected parameters. Colours indicate likelihood values of the samples. The number in each plot shows the Pearson correlation coefficient between the parameter pairs. Diagonal: Marginal distributions obtained with Gaussian kernel estimates. Boxplot whiskers demarcate the 95% percentiles. Below the diagonal: Projected densities in 2D parameter space constructed by 2D Gaussian kernel estimates. The black dots mark the values used to generate the synthetic data.

 $\{\theta_{\mathcal{F}^{TIGd}}, \theta_{\mathcal{F}^{FLAIR}}\} = \{u_c^{TIGd}, u_c^{FLAIR}, \sigma_{\alpha}^2\}. A \text{ normalized FET signal } \hat{\mathbf{y}}^{FET} \text{ has continuous values } y_i^{FET} \in [0,1] \text{ which can be related with the tumor density } u_i \text{ by a Gaussian distribution:}$

$$\mathbb{P}(\hat{\mathbf{y}}^{\scriptscriptstyle FET}|\theta,M) = \prod_{i=1}^{N_{y^{\scriptscriptstyle FET}}^d} \mathbb{P}(y_i^{\scriptscriptstyle FET}|\theta,u_i) = \prod_{i=1}^{N_{y^{\scriptscriptstyle FET}}^d} \mathcal{N}(u_i - b\,y_i^{\scriptscriptstyle FET},\,\sigma^2),$$

where b is an unknown constant of proportionality and σ describes the noise in the FET scan. To eliminate signal from a healthy and necrotic tissue, $N_{y^{FET}}^d$ consists of the voxels included in the T1Gd and FLAIR tumor segmentations, excluding the tumor necrotic core. The FET scan, acquired at $4.3\,mm$ resolution, is interpolated to $1\,mm$ resolution, leading to a correlation length $d=4.3\,mm$. The FET scan introduces two additional unknown parameters $\theta_{\mathcal{F}^{FET}}=\{b,\sigma\}$. The unknown parameters $\theta=\{\theta_u,\theta_{\mathcal{F}^{TIGd}},\theta_{\mathcal{F}^{FLAIR}},\theta_{\mathcal{F}^{FET}}\}$ are assumed independent with uniform prior distribution $\mathbb{P}\left(\theta|M\right)$ given in Supplementary Information (SI).

2. Results

Synthetic data are first used to test the sensitivity of the inference and to show the relevance of multimodal image information for the model calibration. Clinical data are then used to infer patient-specific tumor cell densities and to design personalized RT plans. The personalized and standard RT plans are evaluated based on the tumor recurrence pattern.

A. Sensitivity study. Synthetic data are generated by the glioma model M_u using the BrainWeb anatomy (26) and parameters reported in Table 1. The simulated 'ground-truth' (GT) tumor and the corresponding image observations are shown in Fig. 3. The T1Gd and FLAIR tumor segmentations are constructed by thresholding the GT tumor at $u_c^{T1Gd} = 0.7$

Table 1. The synthetic data are generated with the ground truth (GT) values. The inferred maximum a posterior (MAP) estimate, mean and standard deviation (std) of the marginal distribution of the parameters. The units of time and space are days and mm, respectively.

	D_w	ρ	T	ic_x	ic_y	ic_z	σ	b	u_c^{T1Gd}	u_c^{FLAIR}	σ_{α}^{2}
GT	0.1300	0.0250	302.00	80.64	171.52	128.00	0.0230	0.8800	0.7000	0.2500	-
MAP	0.1226	0.0296	271.13	80.61	171.55	127.92	0.0280	0.9884	0.8440	0.4874	0.0502
mean	0.1543	0.0361	253.85	80.64	171.47	127.80	0.0294	0.9775	0.8325	0.4841	0.0505
std	0.0530	0.0125	107.59	0.1280	0.1024	0.2048	0.0022	0.0139	0.0132	0.0076	0.0004

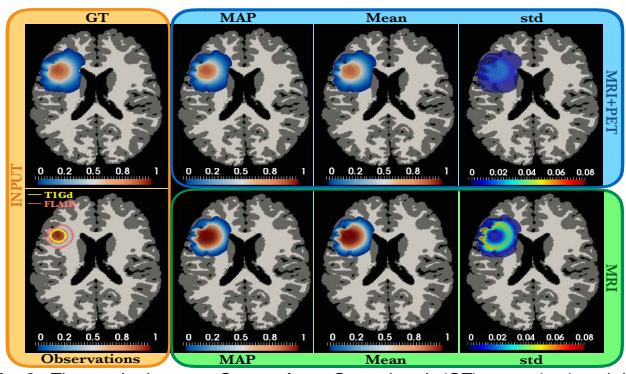


Fig. 3. The synthetic case. Orange box: Ground truth (GT) tumor (top) and the image observations (bottom); Outlines of the T1Gd (yellow) and FLAIR (pink) tumor segmentations, together with the normalised PET signal with additive noise (red-blue color scale). Results of the Bayesian calibration with multimodal data (blue box) are in close agreement with GT data, while calibration based on the binary data only (green box) cannot recover the tumor cell density profile correctly.

and $u_c^{\it FLAIR} = 0.25$. The FET signal is emulated by restricting the GT tumor to the region of the tumor segmentations, adding Gaussian noise with zero mean and standard deviation (std) σ , followed by a normalization. The value of σ is chosen as average std of the FET signal in the healthy brain. Since the synthetic and patient data have the same resolution, the

correlation lengths as specified in Section C are assumed. A sensitivity study for the number of samples per TMCMC generation was performed, indicating that 6000 samples were adequate for the glioma model. The TMCMC procedure converged after 22 generations, forming the posterior probability distribution with manifold shown in Fig. 2 and calibrated parameters reported in Table 1. The inference shows that single time point data does not contain enough information to infer time dependent parameters (D_w, ρ, T) exactly, which is reflected by their high relative std values and strong correlations between them. This is expected, since different combinations of D_w and ρ can generate the same spatial tumor cell density, although at different time points T. Hence, Bayesian inference identifies the distribution of all plausible parameters for the given set of data. At the same time, parameters that affect the tumor spatial pattern, like the initial tumor location (ic_x, ic_y, ic_z) , are identified with high accuracy reflected by their low relative std. The inferred image related parameters $(u_c^{TIGd}, u_c^{FLAIR}, b)$ are slightly overestimated due to the assumed correlation lengths and the effect of the complex brain anatomy. More details about the effect of the anatomy on the tumor cell density are shown in Fig. S1. The inferred σ values are expected to be larger than the GT value, since σ accounts for all sources of discrepancy between the model prediction and image observations, not just the additive noise. Despite the moderate overestimation of image related parameters, the most probable tumor distribution, given as maximum a posteriori (MAP), and the mean tumor distribution, given by

Eq. (5), are almost indistinguishable from the GT tumor (see Fig. 3). The low std (shown in Fig. 3) implies that, with the present Bayesian formulation, the information contained in the multimodal data from a single time point is sufficient to infer the patient tumor cell density.

For comparison, if the model calibration is performed only with the MRI scans, i.e. $\hat{\mathbf{y}} = \{\hat{\mathbf{y}}^{{\scriptscriptstyle TIGd}}, \hat{\mathbf{y}}^{{\scriptscriptstyle FLAIR}}\}$, the inferred tumor cell density varies significantly from the GT tumor as shown in Fig. 3. The reason is that the structural MRI data does not contain information about the tumor density profile. This is also reflected by higher std values inside the tumor region. Nonetheless, the inferred tumor outline is similar to the GT data, since the FET scans do not provide additional information in the regions of lower tumor infiltration. Naturally, the inference with more data yields better results. However, this comparison illustrates the importance of calibrating the tumor model against information from different imaging modalities.

B. Patient study. A retrospective clinical study is conducted on 8 patients diagnosed with GBM. Patients P1-P8 are shown Fig. 4 and the details about the data acquisition are reported in the SI. All patients received the standard treatment, surgery followed by combined radio- and chemotherapy (27). There was no visible tumor after the treatment and patients were regularly monitored for progression. The model M is calibrated against the preoperative scans shown in Fig. 4 (A-D), with the inference results presented in (E-G) and Table S1. The tumor estimates are consistent with the image observations and the low std values imply the high confidence of the inference. These model predictions do not capture the complex tumor internal dynamics, which are certainly more elaborated than described by the simple model M_u . Instead, the calibrated model provides an estimate about possible tumor cell migration pathways in the periphery and surrounding of the tumor, constrained by the patient-specific anatomy and the available tumor observations. As seen in Fig. 4, the model correctly predicts that for patients P1-P4 tumor infiltration is restricted only to one brain hemisphere. Whereas, for patients P5,P7,P8 the model accurately predicts tumor infiltration also inside the healthy-appearing collateral hemisphere. The correctness of these estimates is confirmed by the scans with the first detected tumor recurrence shown in Fig. 4 (H-I). The presence of recurrence in all cases indicates that the population-based treatment is insufficient and the treatment outcome could be improved by personalized dose distribution and escalation plans. The inferred patient-specific tumor cell density can be used to design a customized RT plan. The tumor recurrence pattern is used to assess the benefits of the personalized RT plan over the standard methods. For evaluation purposes, each recurrence scan is registered to preoperative scan using rigid registration which provides a sufficient mapping for most cases. However, it cannot correctly capture tissue displacement around ventricles in patients P7-P8,

making the mapping less accurate in these regions.

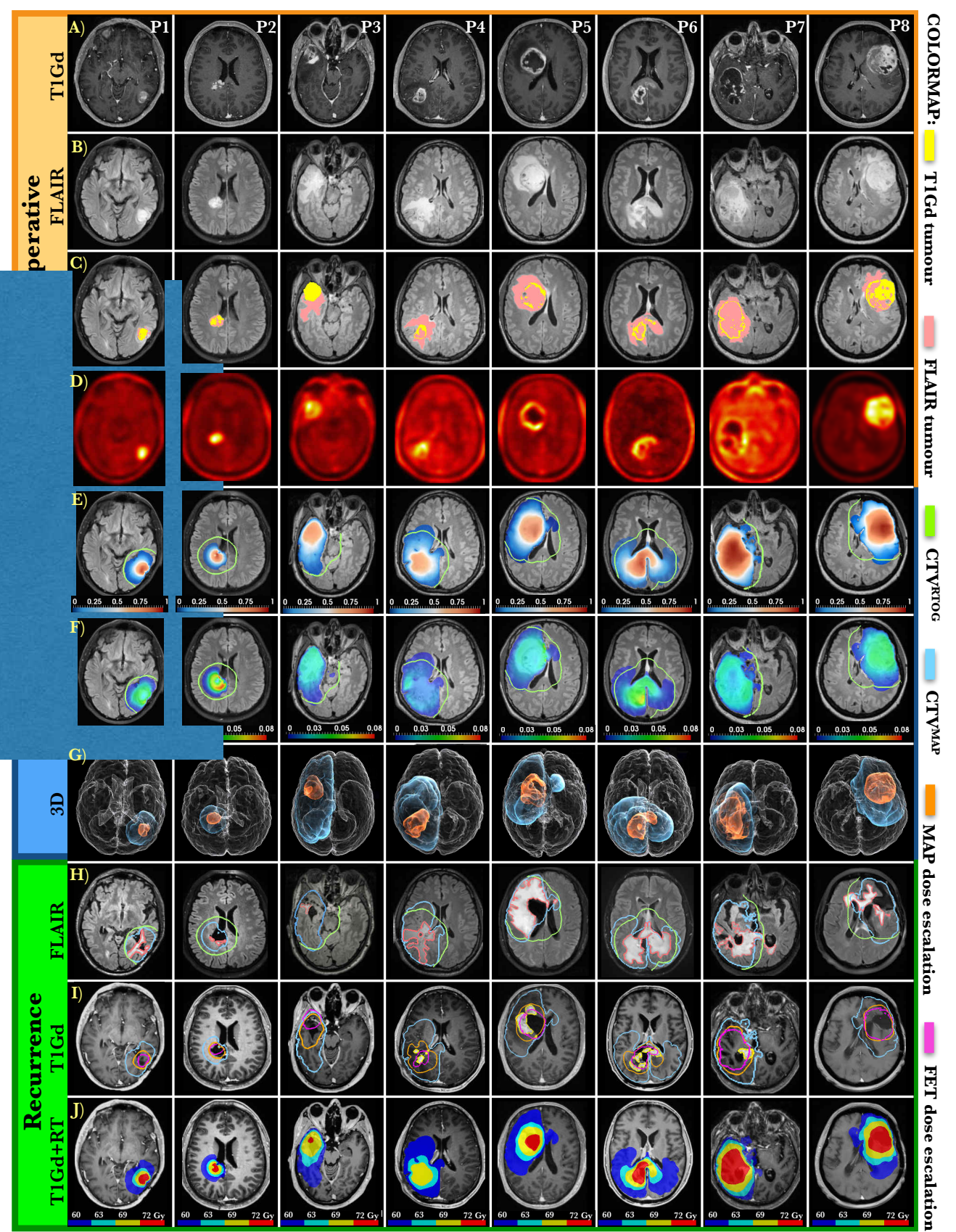


Fig. 4. Results of the Bayesian calibration for patients *P1-P8. Orange box*: Preoperative scans showing (A) T1Gd; (B) FLAIR; (C) Tumor segmentations: T1Gd (yellow) and FLAIR (pink); (D) FET-PET. *Blue box*: (E) MAP and (F) std of the inferred tumor cell densities shown in the preoperative FLAIR scans. The CTV^{RTOG} margin is shown as the green curves. (G). The 3D reconstructions show outlines of the MAP tumor (blue) together with tumor extent visible on the scans (orange) in the preoperative anatomy (white). *Green box*: Scans of the first detected tumor recurrence. (H) FLAIR tumor recurrence (pink), CTV^{RTOG} (green), and CTV^{MAP} (blue) margins. (I) T1Gd tumor recurrence (yellow) and the dose escalation outlines proposed by FET enhancement (magenta) and MAP estimates (orange). (J) Multilevel dose escalation designed by MAP estimates.

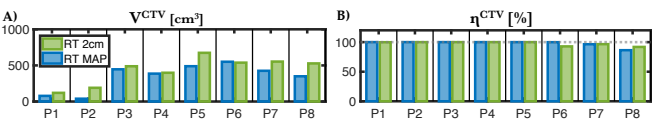


Fig. 5. (A) Overall irradiated volume V^{CTV} designed by the RTOG protocol (green) and MAP inference (blue). (B) Efficiency of the dose distribution η^{CTV} . The CTV^{MAP} use smaller irradiation volume while gaining comparable efficiency as the CTV^{RTOG} .

B.1. Personalized dose distribution. An ideal CTV covers tumor residuals, including invisible tumor infiltration, while sparing healthy tissue. The CTV efficiency, η^{CTV} , defined here as the relative volume of the recurrence tumor (V^{REC}) in the CTV

$$\eta^{CTV} = \frac{|V^{REC} \cap CTV|}{V^{REC}} \times 100\%, \tag{11}$$

is used to assess RT plans. Figure 4 H) shows outlines of the first detected recurrence visible in FLAIR scans (pink lines). The rim of the administrated CTV^{RTOG} , designed by the standard RTOG plan with 2 cm margin around the visible tumor, is marked by the green lines in (E,F,H). A personalized CTV^{MAP} , constructed by thresholding the MAP tumor cell density at u = 0.1% in all patients, is marked by the blue lines in (H-I). A comparison of the treatments displayed in Fig. 5 shows that the personalized CTV^{MAP} spares more healthy tissue, hence reducing radiation toxicity, while maintaining the efficiency of the standard CTV^{RTOG} . In patient P6, the personalized RT plan proposes to irradiate a slightly larger volume, leading to a higher efficiency than the RTOG plan. For patients P7-P8, both the CTV^{RTOG} and CTV^{MAP} show a decrease efficiency, which may be caused by tumor misalignment between preoperative and recurrence anatomy. Nonetheless, the CTV^{MAP} again exhibits a similar efficiency as CTV^{RTOG} , while using a smaller irradiated volume.

B.2. Personalized dose escalation. Since no dose escalation plan for GBM patient has been approved for use in phase III clinical trials, a hypothetical comparison of two escalation plans targeting high tumor cellularity regions is performed. Namely, the dose escalation based on: 1) FET enhancement as pro-

posed in (3) and 2) MAP estimates. We evaluate the efficiency of an escalation plan by its capability of targeting the T1Gdenhanced recurrence tumor, marked by the yellow lines in Fig. 4 I). These are the regions where the recurrent tumor has high cellularity, despite having received the full radiation dose, suggesting radio-resistance. Outlines of the escalation regions designed by FET-enhancement are marked by the magenta lines in Fig. 4 I). The FET-enhancement does not fully cover the T1Gd recurrent tumor in patients P_4 - P_7 , providing a possible explanation for why there is no improvement in progression-free survival observed in (3). Two possible dose escalation plans based on the inferred MAP tumor cell density are shown in Fig. 4: I) a single level dose escalation based on the thresholded MAP solution with threshold u = 30%marked by the orange lines and **J**) cascaded four-level escalation constructed by thresholding the MAP tumor cell density at u = [0.1, 25, 50, 75]%. An optimal design of a MAP based escalation plan would require more extensive study, however these preliminary results show that the inferred high cellularity regions coincide with areas of tumor recurrence better than FET-PET enhancement alone, providing a promising tool for a rational dose escalation design.

3. Conclusion

The presented multimodal Bayesian model calibration framework enables the identification of tumor cell distribution beyond the limitation of the current medical scans. The framework is applicable to more complex tumor growth models and other imaging modalities. Here, we showed that integration of complementary information from morphological and metabolic scans allows to identify tumour cell density from a single time point scans. Patient-specific tumor estimates can be used to design personalized RT plans, targeting shortcomings of standard RT methods. In the future work, the framework will be tested on a larger patient cohort. Nonetheless, the presented results provide a proof of concept that multimodal Bayesian model calibration holds a great promise to assist personalized RT interventions.

- Stupp R, et al. (2014) High-grade glioma: Esmo clinical practice guidelines for diagnosis treatment and follow-up. Annals of Oncology.
- Paulsson AK, et al. (2014) Limited margins using modern radiotherapy techniques does not increase marginal failure rate of olioblastoma. American journal of clinical oncology 37(2):177.
- Piroth M, et al. (2012) Integrated boost imrt with fet-pet-adapted local dose escalation in glioblastomas. Strahlentherapie und Onkologie 188(4):334–339.
- Souhami L, et al. (2004) Randomized comparison of stereotactic radiosurgery followed by conventional radiotherapy with carmustine to conventional radiotherapy with carmustine for patients with glioblastoma multiforme: report of radiation therapy oncology group 93-05 protocol. *International Journal of Radiation Oncology* Biology* Physics* 60(3):853–860.
- Halperin EC, Bentel G, Heinz ER, Burger PC (1989) Radiation therapy treatment planning in supratentorial glioblastoma multiforme: an analysis based on post mortem topographic anatomy with ct correlations. *International Journal of Radiation Oncology* Biology* Physics*.
- Rockwell S, Dobrucki IT, Kim EY, Marrison ST, Vu VT (2009) Hypoxia and radiation therapy past history, ongoing research, and future promise. Current molecular medicine 9(4).
- Combs SE, et al. (2010) Randomised phase i/ii study to evaluate carbon ion radiotherapy versus fractionat ed stereotactic radiotherapy in patients with recurrent or progressive gl iom as: The cinderella trial. BMC cancer 10(1):533.
- Tsien C, et al. (2009) Phase i three-dimensional conformal radiation dose escalation study in newly diagnosed glioblastoma: Radiation therapy oncology group trial 98-03. *International Journal of Radiation Oncology* Biology* Physics* 73(3):699–708.
- Hingorani M, Colley WP, Dixit S, Beavis AM (2012) Hypofractionated radiotherapy for glioblastoma: strategy for poor-risk patients or hope for the future? The British Journal of Radiology.
- Rieken S, et al. (2013) Analysis of fet-pet imaging for target volume definition in patients with gliomas treated with conformal radiotherapy. Radiotherapy and Oncology 109(3):487–492.
- Stockhammer F, et al. (2008) Correlation of f-18-fluoro-ethyl-tyrosin uptake with vascular and cell density in non-contrast-enhancing gliomas. J Neurooncol 88(2):205–10.
- Unkelbach J, et al. (2014) Radiotherapy planning for glioblastoma based on a tumor growth model: improving target volume delineation. *Physics in medicine and biology* 59(3):747.

- Konukoglu E, , et al. (2010) Personalization of reaction-diffusion tumor growth models in mr images: application to brain gliomas characterization and radiotherapy planning.
- Hana L.P. Harpold, Ellsworth C. Alvord KRS (2007) The evolution of mathematical modeling of glioma proliferation and invasion. J Neuropathol Exp Neurol 66(1):1–9.
- Hogea C, et al. (2007) A robust framework for soft tissue simulations with application to modeling brain tumor mass effect in 3d mr images. PHYSICS IN MEDICINE AND BIOLOGY.
- Swan A, et al. (2018) A patient-specific anisotropic diffusion model for brain tumour spread. Bulletin of mathematical biology 80(5):1259–1291.
- Hodgkinson A, , et al. (2018) Computational approaches and analysis for a spatio-structural temporal invasive carcinoma model. *Bulletin of mathematical biology* 80(4):701–737.
- 18. Cristini V, Lowengrub J (2010) Multiscale modeling of cancer. (Cambridge University Press).
- Jackson PR, et al. (2015) Patient-specific mathematical neuro-oncology: using a simple proliferation and invasion tumor model to inform clinical practice. Bulletin of mathematical biology.
- Rockne RC, et al. (2015) A patient-specific computational model of hypoxia-modulated radiation resistance in glioblastoma using 18 f-fmiso-pet. *Journal of the Royal Society Interface*.
 Lê M, et al. (2015) Bayesian personalization of brain tumor growth model in *International*
- Conference on Medical Image Computing and Computer-Assisted Intervention. (Springer).
- Menze B, et al. (2011) A generative approach for image-based modeling of tumor growth in Information Processing in Medical Imaging. (Springer), pp. 735–747.
- Ching J, Chen YC (2007) Transitional markov chain monte carlo method for bayesian model updating, model class selection, and model averaging. *Journal of engineering mechanics*.
- Hadjidoukas P,, et al. (2015) π4u: A high performance computing framework for bayesian uncertainty quantification of complex models. *Journal of Computational Physics* 284:1–21.
- Rossinelli D, et al. (2015) Mrag-i2d: Multi-resolution adapted grids for remeshed vortex meth ods on multicore architectures. *Journal of Computational Physics* 288:1–18.
- Cocosco CA, Kollokian V, Kwan RKS, Pike GB, Evans AC (1997) Brainweb: Online interface
 to a 3d mri simulated brain database in Neurolmage. (Citeseer).
- Stupp R, et al. (2005) Radiotherapy plus concomitant and adjuvant temozolomide for glioblastoma. New England Journal of Medicine 352(10):987–996.

Personalized Radiotherapy Planning for Glioma Using Multimodal Bayesian Model Calibration

Jana Lipková et al. 10.1073/pnas.XXXXXXXXXX

A. Prior PDF. The parameters $\theta = \{\theta_u, \theta_{\mathcal{F}^{TIGd}}, \theta_{\mathcal{F}^{FLAIR}}, \theta_{\mathcal{F}^{FET}}\}$ are assumed independent with uniform prior distribution: $\mathbb{P}(\theta|M) = \prod_{j=1}^{11} \mathbb{P}(\theta_j|M)$, where

$$\mathbb{P}(\theta_j|M) = \frac{1}{\log(\theta_j^{max}) - \log(\theta_j^{min})} \quad for \ \theta_j^{min} \le \theta_j \le \theta_j^{max}, \tag{1}$$

and zero otherwise. The logarithm ensures a similar order of magnitude for prior ranges of all considered parameters, which facilitates the sampling procedure. The prior ranges are chosen as follows: $D_w \in [0.013, 3.8] \, mm^2/day$, $\rho \in [0.0027, 0.19] \, /day$ as reported in (1), $T \in [30, T^{max} + 365] \, day$, where T^{max} is the maximum time that a propagation wave with velocity $v^{min} = 2\sqrt{min(D_w\rho)}$ needs to travel a distance equal to the maximum radius of the visible tumor r^{max} . A prior for the initial location is taken as a cube with a side $2\,r^{max}$, centered at the tumor center of mass. Imaging model parameters are assumed to be $u_c^{T1Gd} \in [0.5, 0.85], \, u_c^{FLAIR} \in [0.05, 0.5], \, \sigma_\alpha^2 \in [0.05, 0.1], \, \sigma \in [0.015, 0.2]$ and $b \in [0.5, 1.02]$. The lower bound for the scaling factor b comes from the fact the T1Gd and FET-PET scans usually do not enhance low grade gliomas, suggesting the same lower bound for the both modalities.

B. Bayesian calibration. Table S1 reports the results of the Bayesian calibration for the clinical data shown in Fig. 4 in the main text

Table S1. Results of the Bayesian calibration for the patient data. Max a posterior (MAP) estimate, mean and standard deviation (std) of the marginal distribution are shown for all the parameters. Time units are reported in days, while spatial units are in mm.

									TICA	FLAIR	9
Cases	D_w	ρ	T	ic_x	ic_y	ic_z	σ	b	u_c^{T1Gd}	u_c^{FLAIR}	σ_{lpha}^2
P1: MAP	0.188	0.029	273.130	0.661	0.692	0.552	0.111	0.959	0.693	0.521	0.051
P1: mean	0.334	0.054	192.649	0.661	0.692	0.550	0.109	0.951	0.712	0.516	0.053
P1: std	0.190	0.031	107.396	0.002	0.002	0.002	0.013	0.040	0.029	0.016	0.002
P2: MAP	0.060	0.024	337.582	0.423	0.618	0.679	0.160	0.846	0.559	0.436	0.051
P2: mean	0.090	0.036	407.101	0.423	0.617	0.679	0.161	0.859	0.577	0.448	0.053
P2: std	0.086	0.034	257.528	0.002	0.001	0.002	0.014	0.055	0.027	0.016	0.003
P3: MAP	0.846	0.010	1094.225	0.441	0.608	0.460	0.218	0.925	0.614	0.347	0.056
P3: mean	0.667	0.008	1468.721	0.437	0.602	0.462	0.214	0.884	0.627	0.352	0.061
P3: std	0.133	0.002	299.056	0.010	0.012	0.008	0.004	0.029	0.011	0.013	0.003
P4: MAP	0.223	0.010	848.498	0.638	0.636	0.716	0.149	1.011	0.796	0.416	0.050
P4: mean	0.227	0.010	1015.395	0.639	0.636	0.716	0.142	1.009	0.793	0.417	0.051
P4: std	0.167	0.007	403.933	0.001	0.002	0.001	0.010	0.009	0.005	0.007	0.000
P5: MAP	2.447	0.107	93.278	0.459	0.432	0.553	0.219	1.020	0.601	0.374	0.051
P5: mean	2.285	0.101	101.387	0.459	0.431	0.552	0.205	1.005	0.609	0.368	0.051
P5: std	0.312	0.014	17.692	0.003	0.002	0.001	0.008	0.013	0.006	0.008	0.001
P6: MAP	0.440	0.029	406.237	0.496	0.654	0.655	0.193	0.937	0.614	0.369	0.052
P6: mean	0.869	0.053	311.425	0.486	0.649	0.652	0.190	0.949	0.642	0.379	0.053
P6: std	0.557	0.033	262.315	0.004	0.004	0.003	0.014	0.040	0.021	0.010	0.002
P7: MAP	0.196	0.007	1580.353	0.636	0.385	0.473	0.218	0.837	0.604	0.362	0.052
P7: mean	0.282	0.010	1204.162	0.638	0.378	0.481	0.213	0.807	0.605	0.359	0.052
P7: std	0.079	0.003	340.776	0.002	0.005	0.004	0.004	0.020	0.004	0.009	0.001
P8: MAP	0.484	0.025	391.577	0.650	0.466	0.626	0.131	0.866	0.602	0.355	0.050
P8: mean	0.689	0.034	353.465	0.649	0.466	0.627	0.130	0.845	0.605	0.355	0.051
P8: std	0.399	0.020	190.028	0.001	0.001	0.001	0.003	0.017	0.003	0.005	0.001

C. Effect of the brain anatomy on the tumor cell density. Patient-specific anatomic restrictions and anisotropic tumor growth result in tumor cell densities that are not constant across the borders of the T1Gd and FLAIR tumor segmentations. Figure S1 (A) shows the distribution of the inferred tumor cell densities across the tumor borders visible in T1Gd and FLAIR scans. The distributions vary significantly along the border and among the patients. This is not surprising, since in the regions of anatomical restrictions, the outlines of the T1Gd and FLAIR tumor segmentations coincide. The effect of the anatomical

restrictions can be alleviated by considering the tumor cell density only at the tumor segmentation outlines far from the ventricles and skull. In this case the inferred tumor cell density varies less and is also more consistent among the patients as shown in Fig. S1 (B). This implies the importance of considering the imaging parameters patient-specific, especially when dealing with complex anatomies such as the brain.

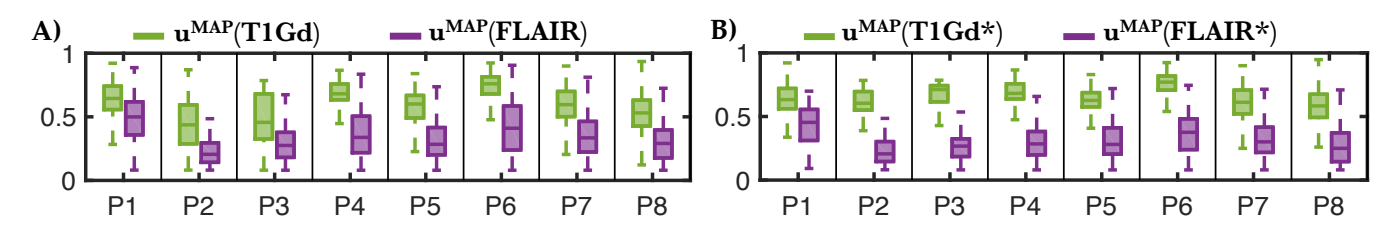


Fig. S1. A) Distribution of the inferred tumor cell densities at the border of the T1Gd (green) and FLAIR (purple) tumor segmentations represented by box plots. B) Distribution of the tumor cell densities at segmentation borders far from anatomical restrictions. Boxplot whiskers demarcate the 95% percentiles.

D. Acquisition protocol. The MRI scans were conducted with 3T mMR Biograph scanner (Siemens Medical Solutions, Germany). FET-PET scans were acquired on a SIEMENS Biograph 64 PET/CT scanner. For standardized metabolic conditions, patients were asked to fast for a minimum of 6h before the PET scan. Intravenous administration of 190 MBq of FET was performed, and low-dose CT (24–26 mAs, 120 kV) for attenuation correction was acquired. Ten-minute PET acquisitions were performed 30 to 40 min post-injection. PET data were reconstructed by filtered back-projection using a Hann filter with corrections for attenuation, scatter, and radioactive decay. All patients provided informed written consent. The study was approved by the ethics committee of the TU Munich and carried out in accordance with the approved guidelines.

1. Hana L.P. Harpold, Ellsworth C. Alvord KRS (2007) The evolution of mathematical modeling of glioma proliferation and invasion. J Neuropathol Exp Neurol 66(1):1-9.